# Numerical Simulation of Realistic High-Speed Inlets Using the Navier-Stokes Equations

Doyle D. Knight*
*Air Force Flight Dynamics Laboratory, Wright-Patterson Air Force Base, Ohio*

**The flowfields of two-dimensional high-speed inlets of realistic engineering geometry are solved through numerical integration of the full Navier-Stokes equations. Two inlets are considered, representative of low-altitude acceleration and high-altitude cruise configurations. The flowfield of each is affected strongly by the curvilinear geometry and shock/boundary-layer interactions. The numerical code solves the full mean compressible Navier-Stokes equations using the algorithm of MacCormack in conjunction with a curvilinear body-oriented coordinate system. Turbulence is represented by a two-layer eddy viscosity model. The computed results compare very favorably with the experimental data.**

## Nomenclature

$e$ = total energy per unit mass
$F$ = vector flux in $x$ direction
$G$ = vector flux in $y$ direction
$M$ = Mach number
$n$ = distance normal to boundary
$p$ = static pressure (mean)
$p_p$ = pitot pressure
$p_t$ = total pressure
$\dot{q}_x, \dot{q}_y$ = total heat-transfer vector components
$Re$ = Reynolds number
$t$ = time
$T$ = static temperature (mass-averaged)
$T_t$ = total temperature
$U$ = vector of dependent variables
$u$ = velocity in $x$ direction (mass-averaged)
$v$ = velocity in $y$ direction (mass-averaged)
$\boldsymbol{u}$ = mean velocity vector
$x,y$ = Cartesian coordinates
$Y'$ = Cartesian coordinate measured from local centerbody surface
$\alpha$ = coefficient of fourth-order numerical damping
$\delta_{BL}$ = computed boundary-layer thickness
$\epsilon$ = turbulent eddy viscosity
$\zeta$ = transformed coordinate
$\eta$ = transformed coordinate
$\lambda$ = second coefficient of viscosity
$\mu$ = molecular viscosity
$\rho$ = density (mean)
$\tau$ = shear stress
$\sigma_{ij}$ = total stress tensor

*Subscripts*

$\infty$ = freestream (upstream of wedge shock)
$e$ = edge of boundary layer
$w$ = wall

## I. Introduction

THE performance of high-speed inlets is often significantly affected by the interaction of the inviscid flow structure and wall turbulent boundary layers. This interaction becomes more critical at higher Mach numbers, where boundary-layer bleed is infeasible due to the high stagnation temperatures. In particular, the interaction between the shock generated by the inlet cowl lip and the inlet centerbody boundary layer requires careful analysis, since the centerbody contours often are designed, for performance reasons, to provide cancellation of the cowl lip shock.[1,2]

Although there has been considerable success in the numerical simulation of shock-wave/boundary-layer interaction, most studies have considered only simple rectilinear geometries.[3-7] Recent experience has indicated the potential for incorporation of a general geometric capability with existing algorithms for solution of Navier-Stokes equations.[8]

The purpose of this research is to demonstrate the feasibility of accurate numerical simulation of high-speed two-dimensional inlets embodying both realistic geometry and strong viscous-inviscid interaction. A smooth body-oriented coordinate system, generated by the method of Thompson,[9] is employed to facilitate handling of the curvilinear flow geometry. The method of MacCormack[3] is utilized to solve the full equations of motion. A similar approach has been applied successfully to the prediction of three-dimensional high-speed corner flow.[10]

To the author's knowledge, the work of Deiwert[11] represents the only other incorporation of a *general* coordinate transformation package with MacCormack's method[3] for the computation of high-speed viscous flows. The formulation, however, differs from that used here in that it solves the integral form of the full equations of motion for each quadrilateral volume element in a mesh of distributed points. The derivatives of the coordinate transformation are computed by separate means depending on the solution operator sequence, resulting in either additional computation time or storage requirements compared to the present method.

## II. Description of Problem

The problem considered is the numerical simulation of the flowfield in a two-dimensional high-speed inlet. Two separate models are considered, as indicated in Fig. 1. Both are two-dimensional designs, exhibiting the significant characteristics of hypersonic inlets, for which extensive experimental data have been collected.[2]

The two models, denoted as P2 and P8, represent inlet configurations typical of acceleration and cruise conditions, respectively, of a hypersonic air-breathing vehicle. They were designed to provide internal compression ratios of 2 and 8, respectively. The forebody wedge, typical of both models, is a nominal 6.5 deg, intended to match a design Mach number of 6 at the inlet entrance under the test conditions of a freestream Mach number of 7.4, allowing for boundary-layer displacement effects. The wedge was cooled, providing a relatively uniform surface temperature of 0.375 $T_{t\infty}$, where the freestream total temperature ($T_{t\infty}$) is 1460°R. The

Received Nov. 22, 1976; presented as Paper 77-146 at the AIAA 15th Aerospace Sciences Meeting, Los Angeles, Calif., Jan. 24-26, 1977; revision received June 27, 1977.

Index categories: Computational Methods; Jets, Wakes, and Viscid-Inviscid Flow Interactions; Supersonic and Hypersonic Flow.

*Captain, U.S. Air Force, and Aerospace Engineer, Flight Mechanics Division; currently at Department of Mechanical Engineering, Rutgers University, Piscataway, N.J. Member AIAA.

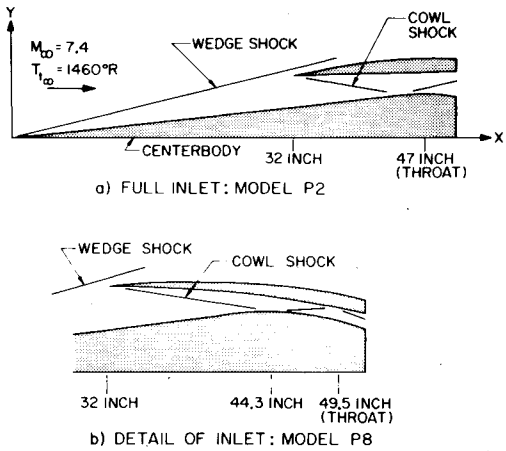


**Fig. 1 Inlet models.**

freestream Reynolds number is $2.7 \times 10^6$/ft, implying that the boundary layer on the centerbody and wedge is turbulent over the majority of its length of approximately 50 in. (see Fig. 1). The transition point was found experimentally to be at approximately 40% of the distance between the wedge leading edge and the inlet entrance.

The cowl was designed with a leading-edge diameter of 0.0449 in., and the cowl was kept at a constant temperature of 0.375 $T_{t_\infty}$. For the P2 inlet, the cowl boundary layer is laminar to the throat; for P8 inlet, the cowl boundary layer transitions approximately halfway between the cowl leading edge and the throat station.

The internal contours were designed with the purpose of providing high total-pressure recovery and approximately uniform static pressure at the inlet throat.[2] Crucial to this concept was the intent of canceling the cowl-generated shock at the centerbody by appropriate design of the centerbody contour. The design procedure of Ref. 2 incorporated an integral boundary-layer method used to predict displacement thickness and a method-of-characteristics program to calculate the inviscid field. (Note that the inviscid flow is supersonic everywhere.) An additional model of the shock/boundary-layer interaction was employed.

The design criterion of shock cancellation at the centerbody was not satisfied experimentally for either model, because of inadequate treatment of the interaction of the cowl-generated shock and the turbulent centerbody boundary layer. The centerbody boundary layer is of considerable size (approximately 15% of the inlet height at the point of intersection of the cowl shock and centerbody), and the interaction with the cowl shock produced a downstream shock pattern that yielded significant nonuniformities in total-pressure recovery at the inlet throat. A subsequent analysis was performed by Seebaugh, using modification of the model of shock/boundary-layer interaction which included the reflected shock wave.[12]

These inlet configurations, then, with their realistic geometry, important viscous-inviscid interactions, and extensive experimental data, provide an excellent opportunity to verify the efficacy of the numerical method and to understand the complex phenomena of high-speed inlets.

## III. Method of Solution

A body-oriented curvilinear coordinate transformation $\zeta(x,y)$, $\eta(x,y)$ is employed to map portions of the $x$-$y$ (physical) plane effectively into the unit square in the $\zeta$-$\eta$ (transformed) plane.[9] A uniform rectilinear grid of points is introduced in the transformed plane, whose image in the physical plane is a highly nonuniform grid capable of resolving the significant features of the flow. In Fig. 2, the two regions involved in the computation of the P2 inlet are

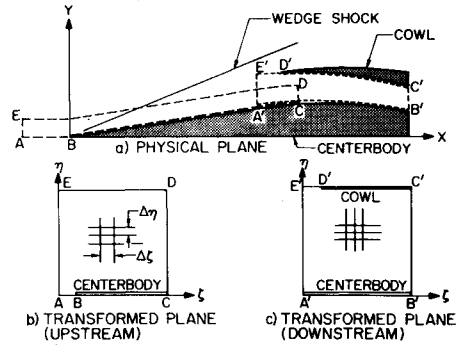


**Fig. 2 Physical and transformed planes.**

shown. The transformation is defined by

$$\nabla^2 \zeta = 0 \tag{1a}$$

$$\nabla^2 \eta = C(\eta)\,(\eta_x^2 + \eta_y^2) \tag{1b}$$

where $\nabla^2 \equiv \partial^2/\partial x^2 + \partial^2/\partial y^2$, $\eta_x = \partial\eta/\partial x$, etc. The factor $C(\eta)$ is constant within the boundary layers, where it provides an approximately geometric stretching of the mesh in the physical plane in a direction nearly normal to the walls. Outside the boundary layers, $C$ is set to zero. The values of $C(\eta)$ are chosen to provide adequate resolution near the wall, as discussed in Sec. IV. In practice, Eqs. (1) are rewritten in terms of $x(\zeta,\eta)$ and $y(\zeta,\eta)$, and solved in the transformed plane with values of $x$ and $y$ specified on the boundaries.[9] The coordinate transformation derivatives then are computed and stored for use with the Navier-Stokes code. The coordinate transformation is applicable to rather general flow geometries and maintains second-order accuracy.

The full mean compressible Navier-Stokes equations utilizing mass-averaged variables,[13] for two-dimensional turbulent flow with no mass, momentum, or energy sources within the flowfield, are the following:

$$\frac{\partial U}{\partial t} + \frac{\partial F}{\partial x} + \frac{\partial G}{\partial y} = 0 \tag{2}$$

where

$$U = \begin{Bmatrix} \rho \\ \rho u \\ \rho v \\ \rho e \end{Bmatrix}; \quad F = \begin{Bmatrix} \rho u \\ \rho uu - \sigma_{xx} \\ \rho uv - \tau_{xy} \\ \rho ue - \dot{q}_x - \sigma_{xx} u - \tau_{xy} v \end{Bmatrix}$$

$$G = \begin{Bmatrix} \rho v \\ \rho uv - \tau_{xy} \\ \rho vv - \sigma_{yy} \\ \rho ve - \dot{q}_y - \tau_{xy} u - \sigma_{yy} v \end{Bmatrix}$$

The total stress tensor, heat-transfer vector, and mean specific total energy $e$ are given in Ref. 4. The equation of state for a thermally perfect gas and Sutherland's viscosity relation are employed. The molecular and turbulent Prandtl numbers are 0.72 and 0.90, respectively.[4]

The turbulent eddy viscosity is given by the two-layer equilibrium model of Cebeci-Smith,[14,15] with the transition model of Dhawan and Narasimha.[16] Details are given in Ref. 17.

The coordinate transformation is incorporated into the equations of motion by rewriting Eq. (2) in terms of the in-

dependent variables $(\zeta,\eta)$. The method of MacCormack is employed to obtain a steady-state solution through integration in time from some initial guess.[8,18] The stress terms are evaluated by appropriate differences in order to retain second-order accuracy throughout.[8] The maximum allowable time step is estimated from the Courant-Friedrichs-Lewy and viscous stability restrictions.[18]

For reasons of economy, the flowfield was subdivided into two and three overlapping regions, respectively, for the P2 and P8 inlets. Beginning with the upstream region, the flow in each region was converged to a steady state. The configuration for the P2 inlet is shown in Fig. 2. The appropriate boundary conditions are applied on the sides of the unit square in the transformed plane. In the upstream region, the conditions are as follows:

1) Centerbody (curve $BC$):

| | |
|---|---|
| $u=v=0$ | (no-slip wall) |
| $T=T_w\cong 0.375\,T_{t\infty}$ | (actual values from Ref. 2) |
| $\partial p/\partial n=0$ | (approximate derived boundary condition; near leading edge a momentum balance was used) |

2) Freestream (curves $AB$ and $EA$):

$$u=u_\infty,\quad v=0,\quad p=p_\infty,\quad T=T_\infty$$

3) Upper surface (curve $DE$): Inviscid equivalent wedge solution utilized downstream of intersection of wedge shock with upper surface.

4) Downstream (curve $CD$): Simple extrapolation of flow variables (i.e., $\partial/\partial x=0$).

In the downstream region, the boundary conditions are as follows:

1) Upstream (curve $A'E'$): Interpolate from computed values in upstream region, with uniform inviscid flow outside centerbody boundary layer given by inviscid wedge shock solution.

2) Centerbody (curve $A'B'$) and cowl (curve $C'D'$):

| | |
|---|---|
| $u=v=0$ | (no-slip wall) |
| $T=T_w\cong 0.375\,T_{t\infty}$ | (actual values from Ref. 2) |
| $\partial p/\partial n$ | (derived from momentum balance at wall) |

3) Upstream of cowl leading edge (curve $D'E'$): Inviscid wedge shock solution.

4) Downstream (curve $B'C'$): Simple extrapolation of flow variables (i.e., $\partial/\partial x=0$).

The end of the mesh (curve $B'C'$) is at least 4 in. downstream (approximately 12 mesh points) of the throat station for both inlets.

## IV. Details of Computation

### A. Geometry and Mesh Distribution

As indicated earlier, the flow geometry is divided into overlapping regions (Fig. 2). Such a procedure is physically sound, since the inviscid region of the flow is supersonic and the boundary layer is developing smoothly at the restart station (e.g., curve $A'E'$).[4] A generous region of overlap (11 points in the $\zeta$ direction) is provided in each case. The regions are as follows: upstream, $-2.46$ in. $\leq x\leq 36.3$ in.; downstream (P2), 29.65 in. $\leq x\leq 51.0$ in.; and downstream (P8), 29.65 in. $\leq x\leq 43.94$ in. (region 1), and 40.0 in. $\leq x\leq 53.78$ in. (region 2). The inlet throat is located at $x=47$ in. for the P2 model and $x=49.5$ in. for the P8 model.

The upstream region consists of a mesh of 64 points in the $\zeta$ direction and 32 points in the $\eta$ direction. The total downstream mesh for each inlet is $70\times 48$ in the $\zeta$ and $\eta$ directions, respectively. The projection of the coordinate transformation $(\zeta,\eta)$ onto the physical $(x\text{-}y)$ plane is a nearly orthogonal curvilinear coordinate system with approximately uniform spacing in the direction of the flow and an exponential spacing in a nearly normal direction within the boundary layers. There are approximately 20 points within the centerbody boundary layer and 8 points within the cowl boundary layer.

Because of the use of no-slip boundary conditions, a particularly fine mesh is required in the vicinity of the wall.[19] Inspection of the model for the turbulent eddy viscosity yields the criterion[17]

$$\Delta n^+\equiv \Delta n(\tau\rho)^{1/2}/\mu \ll 26$$

where $\Delta n$ is the normal distance of the first mesh point away from the wall. Over the centerbody turbulent boundary, $\Delta n^+$ is less than 8.5 for both inlets. The cowl boundary layer is turbulent for the P8 case only and satisfies $\Delta n^+<12.5$.

The cell Reynolds numbers based on velocity and mesh spacing in the two coordinate directions are measures of the ability of a mesh to resolve all of the significant features of the flow.[18] The most significant is that based on the boundary-layer coordinate, which in our instance is

$$Re_\eta\equiv \rho\boldsymbol{u}\cdot\boldsymbol{e}_2\Delta_2/(\mu+\epsilon)$$

where $\boldsymbol{e}_2$ and $\Delta_2$ are the local unit vector and mesh spacing, respectively, in the $\eta$ direction. A generally accepted criterion is that $Re_\eta$ should be less than 2 within the viscous regions (i.e., boundary layers). This criterion is met for the centerbody boundary layer for both inlets. The values of $Re_\eta$ were somewhat larger over the laminar portion of the cowl boundary layers; however, the cowl boundary layer is of minor significance insofar as the overall inlet flow structure is concerned (see Sec V).

For high Reynolds number flows, the values of the cell Reynolds number based on velocity and mesh spacing in the flow direction

$$Re_\zeta\equiv \rho\boldsymbol{u}\cdot\boldsymbol{e}_1\Delta_1/(\mu+\epsilon)$$

are typically much greater than 2, implying that some of the viscous $\zeta$ derivatives are not resolved completely. Experience has shown,[18] however, that such terms are not significant in boundary-layer computations, even for flowfields with strong shock/boundary-layer interactions and Reynolds numbers as high as $10^7$.

Adequate care must be taken, however, to insure adequate streamwise resolution in the regions of shock/boundary-layer interaction. No precise criterion short of the cell Reynolds number argument is known to the author. Experience suggests, however, that for moderate pressure rise (roughly $<2$) and no separation, the wall pressure is rather insensitive to the streamwise mesh spacing within the interaction region provided that the streamwise mesh spacing is less than one-quarter of the interaction width.[18,20] For the P2 inlet, the cowl shock pressure rise is approximately 2.0, and there are six mesh points within the interaction region (44.5 in. $\leq x\leq 46$ in.). The pressure rise on the P8 inlet centerbody is approximately 7.0, due to the cowl shock and internal surface-generated compression; there are five mesh points within this region (44.2 in. $\leq x\leq 46$ in.).

### B. Cowl Lip Flow

For reasons of computational cost, it was not feasible to incorporate sufficient resolution within the downstream mesh (see Fig. 2) to resolve the bluntbody flow in the vicinity of the cowl lip. The bluntbody effects are manifest in two areas. First, there is significant shock curvature in the vicinity of the cowl lip, yielding an effective upstream displacement of the cowl shock compared to that of a sharp leading edge. Second, there is an entropy layer on the cowl generated by the curved shock.

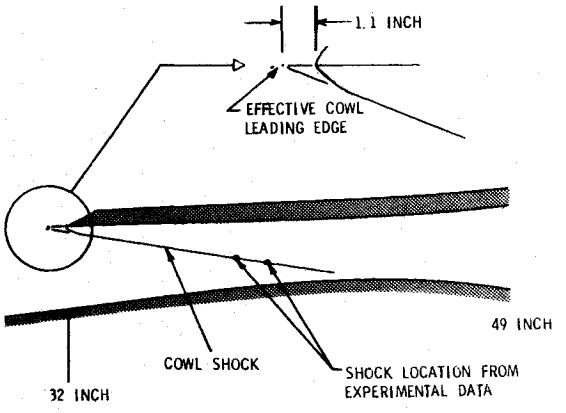


**Fig. 3 Determining effective cowl leading edge.**

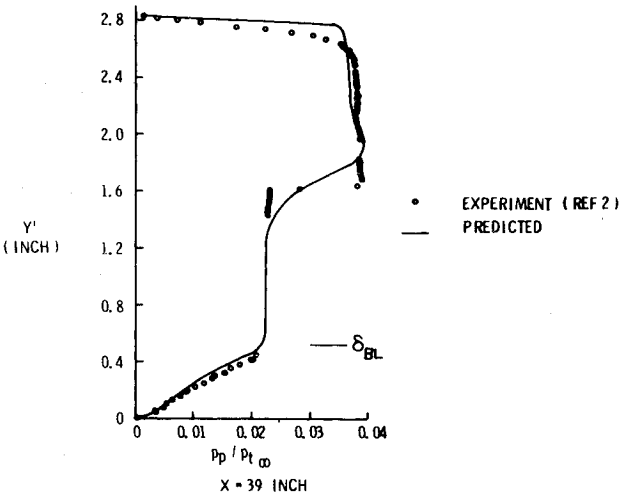


**Fig. 4 Pitot pressure upstream of shock impingement (P2 inlet).**

For both inlets, the effective upstream displacement of the cowl shock is achieved by moving the cowl leading edge to the "virtual origin" defined by the tangent to the cowl surface and the experimental shock location downstream of the inlet entrance (Fig. 3). As the figure indicates, the virtual origin is placed 1.1 in. upstream of the actual origin. Note that this simply effects correct positioning of the cowl shock *ahead* of the interaction and in no manner impairs the dynamics of the shock/boundary-layer interaction itself.

Comparison of numerical and experimental results (see below) indicates that the omission of the cowl entropy layer has a rather minor effect on the predicted flowfield within the inlet for both models and an insignificant effect on computed inlet performance (i.e., flow profiles at the inlet throat). An alternate approach would be to compute the flow locally in the vicinity of the cowl leading edge with a mesh sufficient to resolve the bluntbody effects and to incorporate this solution into the computation of the downstream region.

### C. Numerical Damping

Two types of numerical damping were employed and are described below:

1) Normal stress damping. This technique uses a large positive value of the second coefficient of molecular viscosity $\lambda$ to smooth out starting transients within the flow.[21] As soon as the transients decay, the value of $\lambda$ is reset to the Stokes' value and the calculations continued to steady state.

2) Numerical damping. The fourth-order numerical damping of MacCormack[18] was incorporated into both the $\zeta$ and $\eta$ operators to provide stability in the vicinity of shocks. It should be noted that there is a sign error in the published value for the coefficient $\alpha$ of the damping term.[18] The upstream region was converged with $\alpha = -0.5$. In order to damp out numerical oscillations in the vicinity of the cowl shock, the solutions within the P2 inlet and within region 1 of the P8 inlet were converged with $\alpha = -5.0$. The solution within region 2 of the P8 inlet was converged with $\alpha = -1.1$. The numerical damping is of significance only within the vicinity of the shock wave, where there exists serious truncation error anyway. The effect of the numerical damping is to provide a smooth "smearing" of the shock over several mesh points (see Fig. 4). The numerical damping has an insignificant effect within the boundary layers (including the region of shock/boundary-layer interaction), as was verified by noting that an order-of-magnitude decrease in $\alpha$ within the boundary layer had an insignificant effect upon the computed solution.

### D. Convergence Criteria and Computation Time

For unseparated boundary-layer flows of the type considered, our experience has indicated that the flowfield was converged essentially after a physical time of approximately $2T_c$, where

$$T_c = (\text{length of computation region})/u_\infty$$

in that relative changes in the flow variables over an additional 0.5 $T_c$ (typically 100 time steps) are less than 2%. All regions (see the foregoing) were run to a physical time of at least $2T_c$, except for the upstream region, where the simple nature of the flow permitted $1.5T_c$.

All computations were performed on a CDC-6600. The upstream region required 7.8 hr, whereas the downstream region for the P2 and P8 inlets required 13.2 and 26 hr, respectively. The higher wall pressures in the P8 inlet imply a decrease in viscous sublayer thickness, requiring a finer mesh and consequently larger computation time.

As indicated previously, the primary motivation of this research was to verify the ability of a compressible Navier-Stokes code with coordinate transformation package to predict the complex phenomena of realistic high-speed inlets. For this reason, no major effort was made to decrease computer time. Considerable savings of computer time are possible through use of split-mesh techniques,[18] vector-oriented languages, and assembly language programming.[22] Of greater significance are recent developments that indicate possible one- to two-orders-of-magnitude decrease in computation time through improved algorithms for solution of the compressible Navier-Stokes equations.[23,24]

## V. Results

The upstream region is common to both the P2 and P8 inlets. The computations in this area provide the correct entrance conditions for calculation of the inlet. At the entrance to the inlet ($x = 32$ in.), for example, the computed wall pressure and wall shear stress were within 3.3% and 3.6%, respectively, of the experimental values.

### A. P2 Inlet

The geometry of the P2 inlet was designed to provide cancellation of the cowl shock at the centerbody.[2] Nevertheless, a reflected shock was found experimentally which significantly affected the flow structure at the inlet throat. As will be demonstrated below, the numerical computations clearly reveal these characteristics.

In Fig. 4, the computed pitot pressure is compared with the experimental data at $x = 39$ in., upstream of the intersection of the cowl shock and centerbody. The cowl shock is clearly apparent in both the data and computed results. The computed centerbody boundary-layer thickness $\delta_{BL}$ also is indicated. The predicted results manifest the shock-smearing characteristic of shock-capturing methods.[3,4] It is evident that the omission of the cowl entropy layer has affected the computed profile only in the vicinity of the cowl.

In Fig. 5, the computed pitot pressure at the inlet throat is compared with the experimental data. The circular and triangular symbols represent data taken during two different

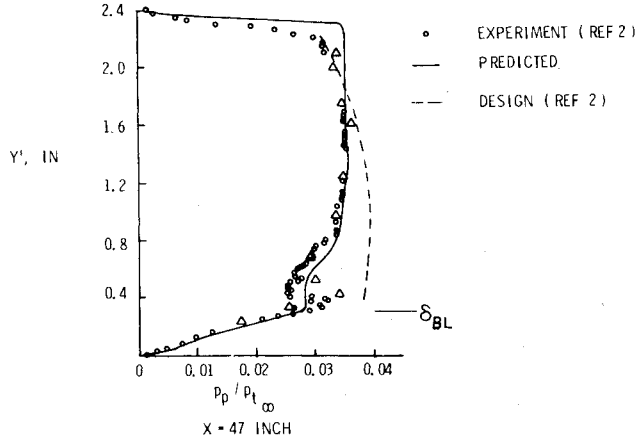


Fig. 5 Pitot pressure at throat (P2 inlet).

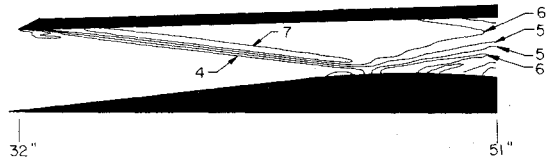


Fig. 6 Isobars (P2 inlet; values of $p/p_\infty$ shown).

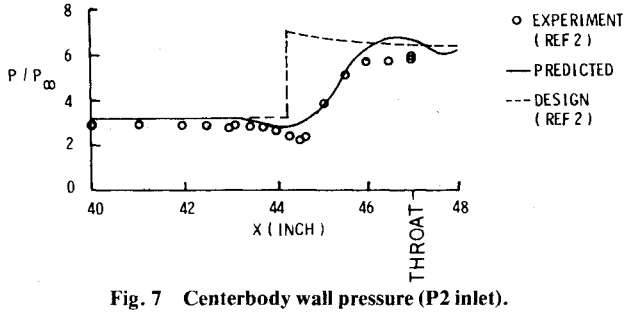


Fig. 7 Centerbody wall pressure (P2 inlet).

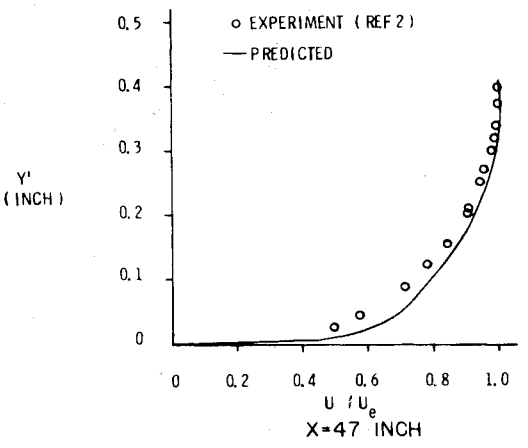


Fig. 8 Centerbody velocity at throat (P2 inlet).

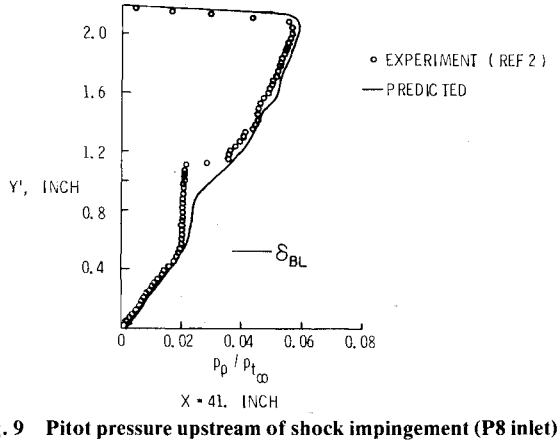


Fig. 9 Pitot pressure upstream of shock impingement (P8 inlet).

tunnel entries; note that a slight change in shock-wave location between tunnel entries is indicated.[2] The dashed line represents the design analysis of Ref. 2, which employed an inviscid method-of-characteristics solution coupled with an integral boundary-layer analysis.

The experimental data in Fig. 5 indicate a reflected shock evident in the sharp change in pitot pressure at $Y' = 0.4$ in. The mesh spacing is not sufficiently fine to resolve this feature. Both the experimental and computed results, however, display an expansion region, associated with the shock/boundary-layer interaction, which is evident in the low pitot pressure between 0.4 and 0.8 in.

In Fig. 6, the computed isobars for the P2 model are indicated. The cowl shock and expansion fan associated with the shock/boundary-layer interaction are clearly evident. In Fig. 7, the predicted centerbody wall pressure is compared with the experimental results. Because of slight nonuniformities in the $y$ direction in the tunnel test-section flow, the experimental centerbody wall pressure drops from 3.07 $p_\infty$ at the inlet entrance ($x = 32$ in.) to 2.91 $p_\infty$ at $x = 40$ in. (ahead of the interaction), although the centerbody contour is straight to $x = 43.4$ in.[2] Thus, at $x = 40$ in., the computed wall pressure is 8% higher than the experimental value, compared to 3.3% higher at the inlet entrance. Between $x = 43$ and 44.5 in., a slight expansion, due to centerbody surface turning, is evident in both experimental and predicted profiles.

The rapid wall pressure rise caused by the impingement of the cowl shock is clearly shown. At the throat ($x = 47$ in.), the computed wall pressure is 11% above the experimental value. This discrepancy may be attributed basically to the omission of effects of tunnel flow nonuniformity, the utilization of a turbulence model designed for equilibrium turbulent flows in a flowfield with strong interaction, and numerical truncation error.

Both the computed and experimental cowl pressures display a nearly uniform behavior between the cowl leading edge and the throat, due to the nature of the inlet goemetry (see Fig. 1) and the fact that the reflected shock impinges the cowl downstream of the throat. The computed cowl pressure is within 9% of the experimental values at all stations.

The velocity profile in the centerbody boundary layer at the inlet throat is shown in Fig. 8, where the velocity at the edge of the boundary layer is $u_e = 3819$ fps. The computed profile indicates a slightly greater velocity in the inner region of the boundary layer. Agreement between computed and measured centerbody velocity profiles ahead of the shock/boundary-layer interaction (not shown) is excellent. There is no boundary-layer separation for either inlet, in agreement with experimental results.[12]

### B. P8 Inlet

The internal contours of the P8 inlet were designed by the methods of Ref. 2 to provide cancellation of the cowl shock at the centerbody and an isentropic compression to the throat (see Fig. 1). As with the P2 inlet, cancellation of the cowl shock at the centerbody was not achieved. A reflected shock was obtained which intersected the cowl upstream of the throat.

In Fig. 9, the predicted and experimental pitot pressures are shown at $x = 41$ in., approximately 3 in. upstream of the intersection of the cowl shock with the centerbody. The agreement is very good. The design profile (not shown) of Ref. 2 is also in good agreement. Again, the cowl shock is apparent in the steep rise in pitot pressure at $Y' = 1.1$ in. The

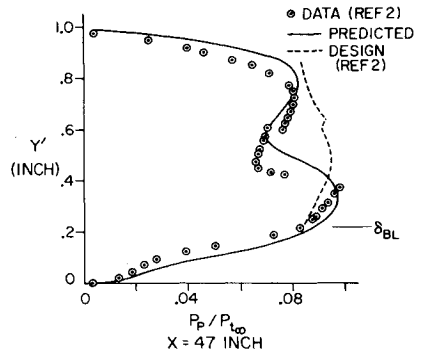


**Fig. 10 Pitot pressure at station between shock impingement and throat (P8 inlet).**

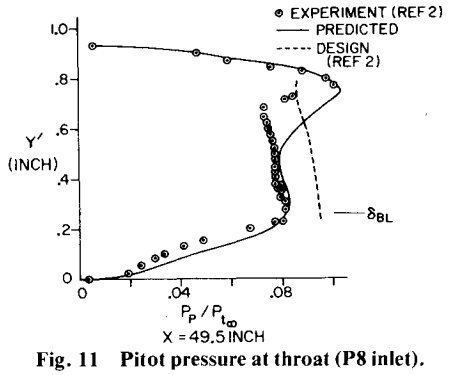


**Fig. 11 Pitot pressure at throat (P8 inlet).**

flow compression due to the cowl surface curvature is apparent in the gradient in the pitot pressure between 1.1 in. and 2.0 in.

The flow structure immediately downstream of the cowl shock/centerbody boundary-layer interaction is evident in Fig. 10, where predicted and measured pitot pressure are displayed at $x = 47$ in., approximately 3 in. downstream of the interaction. Again, the agreement is good. The dashed line represents the design analysis of Ref. 2. The reflected shock is at $Y' = 0.4$ in., as evidence by the abrupt decrease in pitot pressure at that location. The effects of flow compression again are visible in the region between 0.4 and 0.8 in. As in the P2 case, the effects of the omission of the cowl entropy layer are seen to be confined to the vicinity of the cowl.

The inlet performance is shown in Fig. 11, where predicted and measured pitot pressures are shown at the inlet throat ($x = 49.5$ in.). The agreement is good. Again, the design analysis of Ref. 2 is indicated by the dashed line. The initial cowl shock interacts with both the centerbody boundary layer (at $x = 44$ in.) and cowl boundary layer (at $x = 48.5$ in.) and is apparent at the throat at $Y' = 0.7$ in.

In Fig. 12, the predicted and measured values of centerbody wall pressure are displayed. As mentioned earlier, the predicted wall pressure ahead of the interaction exceeds the measured value by about 8%. The sharp pressure rise associated with cowl shock impingement is evident. The computed pressure at the throat is approximately 15% too high, which may be attributed basically to omission of effects of tunnel nonuniformity, limitations of the turbulence model, and numerical truncation error.

The details of the wall pressure on the cowl are shown in Fig. 13. The computed results indicate the flow compression and impingement of the reflected shock on the cowl. The expansion ahead of the reflected shock impingment is a feature associated with the shock/boundary-layer interaction on the centerbody and is apparent in the numerical results. Oscillations in the computed wall pressure are evident in the region between 45 and 47 in. and are believed to be numerical in origin. Further work is needed to understand this localized

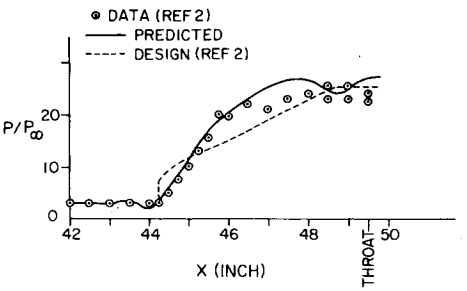


**Fig. 12 Centerbody wall pressure (P8 inlet).**

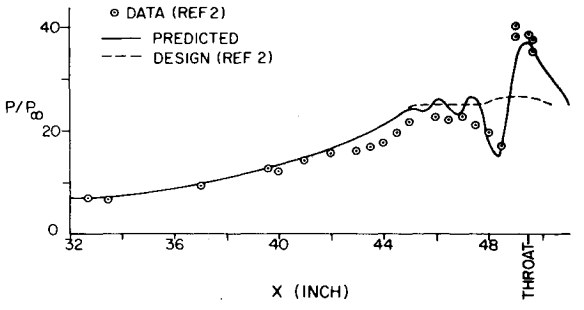


**Fig. 13 Cowl wall pressure (P8 inlet).**

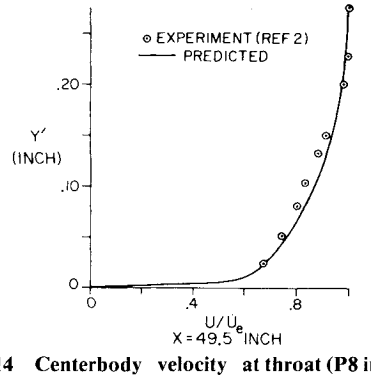


**Fig. 14 Centerbody velocity at throat (P8 inlet).**

behavior. The design curve of Ref. 2 also is shown. The computed and measured velocity profiles in the centerbody boundary layer at the inlet throat are indicated in Fig. 14.

## VI. Conclusions

The feasibility of accurate numerical simulation of high-speed two-dimensional inlets embodying realistic engineering geometries and strong viscous-inviscid interaction has been demonstrated. The procedure involves integration of the full mean compressible Navier-Stokes equations using MacCormack's method combined with a body-oriented coordinate transformation package.

Two inlet configurations, representative of low-altitude acceleration and high-altitude cruise conditions of high-speed air-breathing vehicles, have been considered. The performance of each inlet is affected significantly by the interaction of the cowl-shock and wall boundary layers.

The numerical results compare very favorably with the experimental data. In particular, the computations indicate the existence of a reflected shock emanating from the intersection of the cowl-shock and centerbody turbulent boundary layer. Although the inlet contours had been designed to avoid the formation of such a reflected shock, the reflected shock nonetheless was evident in the experimental data. Detailed comparison between experimental and predicted pitot pressure and velocity profiles is also very favorable.

## Acknowledgments

The author is grateful to D.S. McRae, Wilbur Hankey Jr., and Joseph Shang for their assistance in the course of this investigation.

## References

[1] Wasserbauer, J.F. and Choby, D.A., "Performance of a Bicone Inlet Designed for Mach 2.5 with Internally Distributed Compression and 40 Percent Internal Contraction," NASA TM X-2416, Feb. 1972.

[2] Gnos, A.V., Watson, E.C., Seebaugh, W.R., Sanator, R.J., and DeCarlo, J.P., "Investigation of Flow Fields within Large-Scale Hypersonic Inlet Models," NASA TN D-7150, April 1973.

[3] MacCormack, R.W., "Numerical Solution of the Interaction of a Shock Wave with a Laminar Boundary Layer," *Lecture Notes in Physics,* Vol. 8, 1971, pp. 151-163.

[4] Shang, J.S., Hankey, W.L., Jr., and Law, C.H., "Numerical Simulation of Shock Wave-Turbulent Boundary-Layer Interaction," AIAA Paper 76-95, Washington, D.C., 1976.

[5] Carter, J.E., "Numerical Solutions of the Navier-Stokes Equations for the Supersonic Laminar Flow over a Two-Dimensional Compression Corner," NASA TR R-385, July 1972.

[6] Hung, C.M. and MacCormack, R.W., "Numerical Solutions of Supersonic and Hypersonic Laminar Compression Corner Flows," *AIAA Journal,* Vol. 14, No. 4, April 1976, pp. 475-481.

[7] Shang, J.S. and Hankey, W.L., Jr., "Numerical Solution for Supersonic Turbulent Flow over a Compression Ramp," *AIAA Journal,* Vol. 13, No. 10, Oct. 1975, pp. 1368-1374.

[8] Knight, D.D. and Hankey, W.L., Jr., "Numerical Simulation of Nonchemically Reacting Radial Supersonic Diffusion Laser," AIAA Paper 76-60, Wash. D.C.., Jan. 1976.

[9] Thompson, J.F., Thames F.C., and Mastin, C.W., "Automatic Numerical Generation of Body-Fitted Curvilinear Coordinate System for Field Containing any Number of Arbitrary Two-Dimensional Bodies," *Journal of Computational Physics,* Vol. 15, March 1974, pp. 299-319.

[10] Shang, J.S. and Hankey, W.L., Jr., "Numerical Solution of the Compressible Navier-Stokes Equations for a Three-Dimensional Corner," AIAA Paper 77-169, Los Angeles, Jan., 1977.

[11] Deiwert, G.S., "Numerical Simulation of High Reynolds Number Transonic Flows," *AIAA Journal,* Vol. 13, No. 10, Oct. 1975, pp. 1354-1359.

[12] Seebaugh, W.R., "Hypersonic Flows in Large-Scale Inlet Models," *Journal of Aircraft,* Vol. 10, Jan. 1973, pp. 38-44.

[13] Rubesin, M.W. and Rose, W.C., "The Turbulent Mean-Flow Reynolds-Stress, and Heat-Flux Equations in Mass-Averaged Dependent Variables," NASA TM X-62, 248, March 1973.

[14] Cebeci, T., Smith, A.M.O., and Mosinskis, G., "Calculations of Compressible Adiabatic Turbulent Boundary Layers," *AIAA Journal,* Vol. 8, Nov. 1970, pp. 1974-1982.

[15] Cebeci, T., "Calculations of Compressible Turbulent Boundary Layers with Heat and Mass Transfer," *AIAA Journal,* Vol. 9, June 1971, pp. 1091-1097.

[16] Harris, J.E., "Numerical Solution of the Equations for Compressible Laminar, Transitional and Turbulent Boundary Layers and Comparison with Experimental Data," NASA TR T-368, 1971.

[17] Knight, D.D., "Numerical Simulation of Realistic High-Speed Inlets Using the Navier-Stokes Equations," AIAA Paper 77-146, Los Angeles, Jan. 1977.

[18] MacCormack, R.W. and Baldwin, B.S., "A Numerical Method for Solving the Navier-Stokes Equations with Application to Shock-Boundary Layer Interactions," AIAA Paper 75-1, Jan. 20-22, 1975.

[19] Shang, J.S., "Computation of Hypersonic Turbulent Boundary Layers with Heat Transfer," *AIAA Journal,* Vol. 12, No. 7, July 1977. pp. 883-884.

[20] Rose, W.C., "Practical Aspects of Using Navier-Stokes Codes for Predicting Separated Flows," AIAA Paper 76-96, Wash. D.C.

[21] McRae, D.S., "A Numerical Study of Supersonic Viscous Cone Flow at High Angle of Attack," AIAA Paper 76-97, Wash. D.C., 1976.

[22] Deiwert, G.S., "Simulation of Turbulent Transonic Separated Flow Over an Airfoil," *NASA Conference on Aerodynamic Analyses Requiring Advanced Computers,* NASA SP-347, 1975, pp. 419-436.

[23] MacCormack, R.W., "An Efficient Numerical Method for Solving the Time-Dependent Navier-Stokes Equations at High Reynolds Number," NASA TM X-73, 129, July 1976.

[24] Shang, J.S., "An Implicit-Explicit Method for Solving the Navier-Stokes Equations," AIAA Paper 77-646, Albuquerque, N. Mex., June 1977.